

GNSS-Independent and Obstacle Avoidance for UAVs Using a Compact 360° Scanning Head

Name omitted for review

Dept name omitted for review

Organization name omitted for review

City, Country omitted for review

Email address omitted for review

Name omitted for review

Dept name omitted for review

Organization name omitted for review

City, Country omitted for review

Email address omitted for review

Name omitted for review

Dept name omitted for review

Organization name omitted for review

City, Country omitted for review

Email address omitted for review

Name omitted for review

Dept name omitted for review

Organization name omitted for review

City, Country omitted for review

Email address omitted for review

Name omitted for review

Dept name omitted for review

Organization name omitted for review

City, Country omitted for review

Email address omitted for review

Name omitted for review

Dept name omitted for review

Organization name omitted for review

City, Country omitted for review

Email address omitted for review

Abstract—We develop and evaluate a GNSS-independent guidance, navigation, and collision-avoidance stack for a multicopter that pairs SLAM with an omnidirectional obstacle sensor built from a compact 360° scanning head. The head rotates a single-beam range sensor via a stepper and slip ring with Hall indexing, and its detections are translated into small roll/pitch overrides using a simple distance-to-PWM rule with a 0.70 m safety radius. We test the system in two settings that stress different failure modes: a reflective-wall box arena that exposes specular and multipath effects, and a software-in-the-loop scene that exercises drift and loop-closure recovery. In the arena, LiDAR provided tighter polar occupancy and higher repeatability than ultrasound; within ≈ 1.05 m, LiDAR errors were typically $<10\%$ while ultrasound often exceeded 30% . In the city-canyon runs, loop closures at intersections pulled trajectories back to the street grid and kept drift bounded over multi-block paths. Together these results show that a lightweight, compute-efficient sensing and control pipeline can deliver reliable mapping and safe evasive maneuvers without GNSS or a ground station, making it practical for cluttered, denial-prone environments.

Keywords—Unmanned aerial vehicles, SLAM, LiDAR, SONAR, omnidirectional sensor.

I. INTRODUCTION

Unmanned Aerial Vehicles (UAVs) are increasingly employed in missions that demand autonomous and reliable operation, including disaster response, surveillance, precision agriculture, and environmental monitoring [1], [2], [3], [4], [5], [6]. A fundamental requirement for such missions is accurate Guidance, Navigation, and Control (GNC). Traditionally, UAV navigation has relied heavily on Global Navigation Satellite Systems (GNSS). However, in practice, UAVs are frequently forced to operate in GNSS-denied or degraded environments due to multipath interference, urban obstructions, adverse weather, or intentional jamming and spoofing [7], [8], [9]. These limitations necessitate the development of alternative, self-reliant navigation and control strategies.

From a technical perspective, GNSS denial presents multiple challenges. First, state estimation becomes unreliable when position updates are lost. Inertial Measurement Units (IMUs) can bridge short-term gaps, but error accumulates rapidly due to bias drift [10]. Second, environmental perception is hindered by sensor limitations: LiDAR performance is degraded in heavy rain or fog, SONAR suffers from multipath echoes, and vision-based systems are sensitive to illumination changes [11], [12]. Third, environmental interaction introduces aerodynamic disturbances near walls,

tunnels, or confined spaces that complicate flight stability [9]. Finally, the computational burden of simultaneous localization and mapping (SLAM) and sensor fusion algorithms often exceeds the onboard processing power of small UAVs, forcing a trade-off between real-time performance and accuracy [13], [14].

To address these challenges, Simultaneous Localization and Mapping (SLAM) has emerged as a promising navigation paradigm. SLAM allows a UAV to incrementally build a map of its environment while simultaneously estimating its own trajectory within that map [15], [16]. Recent developments in graph-based SLAM, visual-inertial odometry, and LiDAR-based loop closure have significantly improved robustness and accuracy [17], [18], [19]. However, deploying SLAM on lightweight UAV platforms requires efficiency in algorithm design, sensor data fusion, and error correction strategies.

In addition to navigation, obstacle avoidance and motion planning are critical components of UAV autonomy. Techniques such as Control Barrier Functions (CBFs) have demonstrated potential in enforcing safety constraints while maintaining performance in dynamic environments [20], [21]. CBF-based controllers can be integrated into quadratic programming frameworks, ensuring that safety constraints (e.g., collision avoidance) are never violated even under uncertainties in state estimation. This is particularly valuable when UAVs must maneuver through GNSS-denied and cluttered environments where dynamic re-planning and fast obstacle detection are essential.

Bangladesh provides a particularly relevant case study for such developments. UAVs are already being applied in tasks such as flood modeling in the Jamuna floodplain [4], urban mapping in Dhaka [2], air quality monitoring [3], topographic surveys [1], and precision agriculture [6]. However, these missions are often carried out in environments where GNSS reliability is compromised—dense urban settlements, metallic infrastructures, or during extreme weather conditions [5], [7]. Moreover, sensitive facilities require UAV operations in jamming-prone zones, making GNSS-independent solutions not just advantageous but essential [8].

Indoor micro-UAVs often rely on budget ultrasonics with wide lobes and multipath sensitivity, leading to unstable sector decisions. LiDAR remedies angular selectivity but adds compute and integration costs. What is missing is a compact, reproducible pipeline that quantifies these tradeoffs and maps distance to bounded PWM overrides. This paper contributes: (i) a compact 360° scanning head with a sectorized distance-to-PWM hazard law for roll/pitch override; (ii) a controlled,

reflective-arena comparison of LiDAR vs sonar accuracy, repeatability, and scan-to-map convergence; and (iii) a city-canyon 2D LiDAR SLAM validation illustrating drift behavior and loop-closure recovery under turns. This paper focuses exclusively on GNSS-denied indoor avoidance and mapping on an UAV in GNSS-denied environments relevant to both global applications and the unique challenges of Bangladesh.

II. METHODOLOGY

We target autonomous collision avoidance for a quadrotor operating in GNSS-denied environments. The system in fig. 1 is modeled as a closed-loop with (i) a plant (rigid body + propulsion), (ii) proprioceptive/exteroceptive sensors, and (iii) a flight controller receiving real-time obstacle cues from an onboard microcontroller. The objective is to convert single-beam, uni-directional range sensors (ultrasonic and LiDAR) into a 360° situational awareness pipeline and to map detections into roll/pitch RC channel overrides that command evasive motion.

To obtain 360° coverage with minimal mass and cost, we designed a compact scanning head in SolidWorks, shown in fig. 2. A stepper motor drives the sensor carriage via a small pulley pair; a through-bore slip ring routes signal to the rotating sensor, eliminating cable twist. A home index (magnet + Hall sensor) defines the zero-bearing. The bearing resolution is set by the motor step angle and gearing. With step size and pulley ratio ρ , the per-sample bearing increment is

$$\Delta\psi = \frac{360^\circ}{N_{\text{rev}} \rho} \quad (1)$$

where N_{rev} is steps per revolution of the motor. We calibrate $\psi = 0^\circ$ at the Hall index and use cumulative stepping to cover $[0^\circ, 360^\circ)$.

We evaluate two single-beam sensors mounted on the scanning head:

- Ultrasonic SONAR (time-of-flight): distance D with speed of sound corrected for ambient temperature.
- Single-point LiDAR (time-of-flight): internal timing yields distance with typical mm-cm repeatability.

Each rotation produces a set $\{(\psi_i, D_i)\}$. A time-synchronized logger records (ψ, D) , raw echo quality, and flight-control timestamps. We define a maximum permissible range $D_{\text{safe}} = 70$ cm. Any validated return with $D \leq D_{\text{safe}}$ flags a sector hazard



Fig. 1. Airborne architecture with sensor mounted

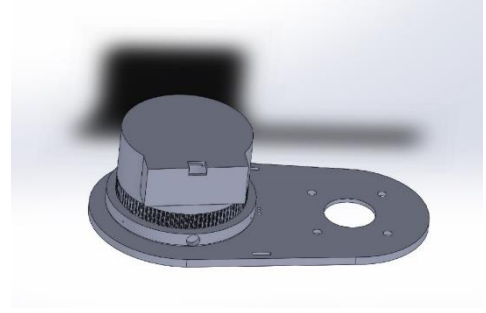


Fig. 2. CAD Model of sensor head

Azimuth is partitioned into four sectors (front $[315, 45]$, left $[45, 135]$, rear $[135, 225]$, right $[225, 315]$). The most threatening sector at time t is the one with minimum validated D . We map proximity to PWM with a bounded ramp:

$$u(t) = \text{clip}(1500 \pm k[D_{\text{safe}} - D(t)], u_{\text{min}}, u_{\text{max}}) \quad (2)$$

where '+' selects the axis that moves the vehicle away from the obstacle (e.g., front \rightarrow pitch-back > 1500 , left \rightarrow roll-left < 1500). Hysteresis prevents oscillation at the sector boundaries. MAVLink RC_CHANNELS_OVERRIDE is streamed until no hazards persist.

The UAV guidance and control framework was validated using a simulation environment developed in MATLAB Simulink, integrated with Unreal Engine for 3D visualization. The system architecture was modeled through interconnected Simulink blocks in fig. 3. Translational inputs were applied in the global frame, and rotational states were expressed in ZYX Euler angles. Ramp and constant signals were used to generate forward motion while maintaining altitude and stability.

Environmental perception was achieved using a 2D LiDAR sensor block, producing point cloud data for obstacle detection and mapping. The captured data was processed and visualized to represent the UAV trajectory and obstacle distribution in fig. 4.

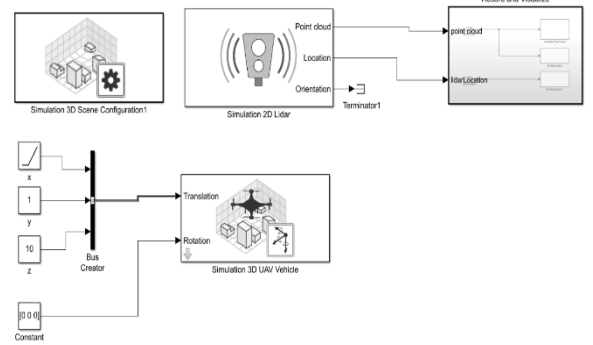


Fig. 3. Simulink Setup Block for the SLAM simulation

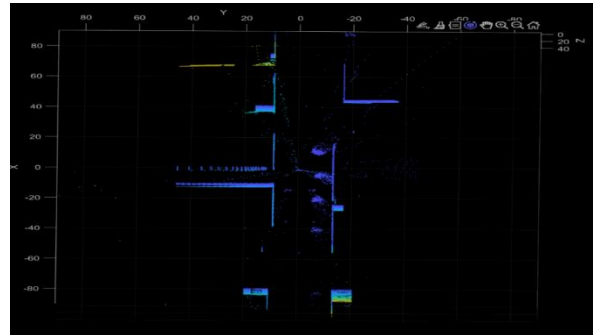


Fig. 4. Point Cloud Data Generation

We evaluated the sensors in a purpose-built reflective box arena in fig. 5 with smooth inner walls to emulate hard-wall reflections. The enclosure’s internal clear span was $[L \times W \times H = \text{cm}]$. A flat-panel obstacle set was mounted at pre-measured bearings and radii (tape-measured ground truth), and the scanning head was placed at the geometric center with its rotation axis vertical. For each configuration we recorded N_{rev} complete revolutions (typically 3–5 per sensor), logging synchronized bearing–range tuples with timestamps and the device-reported echo-quality flag. Reference distances and angles to the panels were measured with a tape immediately before each run and used both for plotting and computing percentage error per iteration. This setup isolates detection geometry and reflection artefacts while providing repeatable ground truth for LiDAR–ultrasonic comparisons.



Fig. 5. Reflective box arena for LiDAR and SONAR tests

III. RESULT AND DISCUSSION

The scanning head was mounted at the arena center with the rotation axis vertical and the sensor height aligned to the panel plane. Reference bearings for the flat panels were tape-measured prior to each run and the hazard threshold used by the avoidance logic was $D_{\text{safe}} = 0.70 \text{ m}$.

For completeness we visualize the control law that converts nearest-obstacle distance into RC channel overrides (used in both simulation and hardware tests). Fig. 6 displays the curve and active region $D \leq D_{\text{safe}}$ for a reference situation.

To make the perception-to-actuation interface explicit, Table I lists which sector triggers which axis, the PWM polarity, and the command semantics. Proximity bands are shown as design-derived ranges.

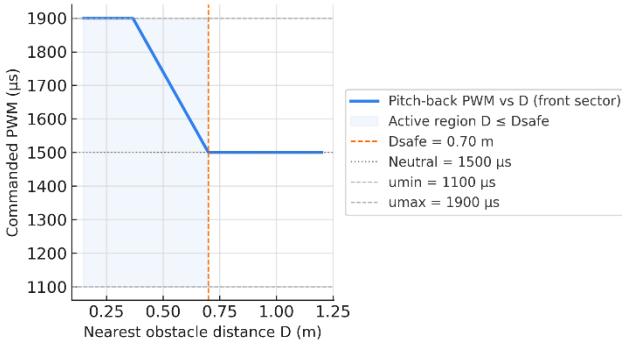


Fig. 6. PWM override vs nearest-obstacle distance

TABLE I. SECTORIZED DISTANCE TO PWM HAZARD LAW

Sector (bearing)	Proximity Band (D)	PWM Range	Command Semantics
Front [315°, 45°]	<0.35 m	1850–1900	Nose-up / Back-off
	0.35–0.55 m	1650–1800	
	0.55–0.70 m	1520–1600	
Left [45°, 135°]	<0.35 m	1100–1150	Translate Left
	0.35–0.55 m	1200–1350	
	0.55–0.70 m	1400–1480	
Rear [135°, 225°]	<0.35 m	1100–1150	Nose-down / Advance
Right [225°, 315°]	<0.35 m	1850–1900	Translate Right

Fig. 7 and 8 plot single-ping ranges in polar form over a 360° sweep (0° forward, clockwise). Both sensors recover the two dominant obstacle arcs in the box test, yet their angular continuity and spurious-return behavior differ.

Fig. 7 recovers the same arcs but as fragmented bands with scattered points and occasional saturations and outliers are frequent. Angular continuity is poorer, reflecting step-like range changes and multipath-induced jumps. Fig. 8 forms two continuous, high-density arcs with only rare excursions. Across 352 pings the radial spread is moderate and outliers are negligible. The angular smoothness is consistent, indicating few abrupt jumps between adjacent bearings.

In this confined environment, LiDAR yields a coherent angular map with minimal false returns, whereas the ultrasonic sensor exhibits higher spurious-return rate and abrupt bearing-to-bearing changes. These characteristics align with the time-series results and explain why LiDAR provides a more reliable input for obstacle avoidance.

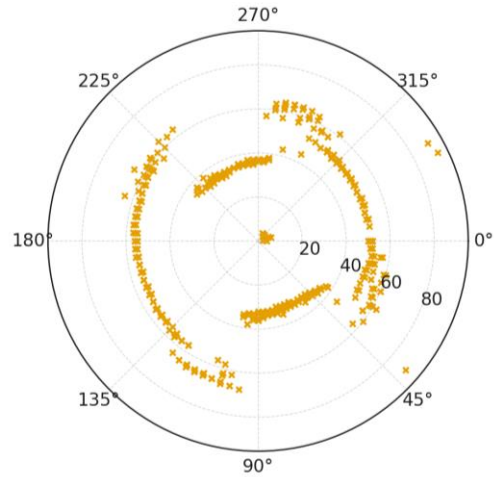


Fig. 7. Ultrasonic sensor obstacle detection map (polar).

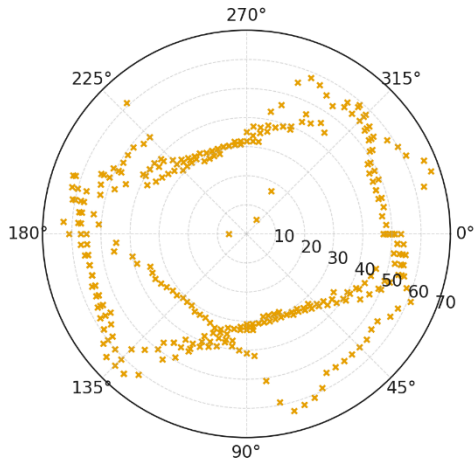


Fig. 8. LiDAR Obstacle Detection map (polar)

Fig. 9 and 10 show the raw obstacle range over sequential iterations. Both sensors trace the expected near-far cycling of the obstacle field ($\approx 30\text{--}65\text{ cm}$), but their temporal behavior differs markedly.

Fig. 9 produces a smooth, repeatable waveform with few discontinuities. Across 352 samples the range is $44.4 \pm 11.3\text{ cm}$ (mean \pm SD) and median 45 cm. Pathological outliers are rare: 2/352 ($<1\%$) readings fall below 10 cm and none exceed 80 cm.

Fig. 10 exhibits the same gross near-far pattern but with step-like plateaus, frequent discontinuities and occasional saturations. Over 487 samples the range is $47.8 \pm 13.8\text{ cm}$ and median 51 cm. Outliers are common: 15/487 (3%) readings $<10\text{ cm}$ and 3/487 (0.6%) $>80\text{ cm}$, including spikes approaching 90 cm.

While both sensors capture the scene's periodic geometry, LiDAR maintains continuity and rejects spurious returns much more effectively. The SONAR trace shows repeated dropouts and saturations that would propagate into the controller as jittery distance cues, whereas the LiDAR signal remains within the operational band (30–65 cm) with only rare excursions. Combined with the error-percentage plots, these time-series confirm LiDAR as the more reliable ranging input for obstacle avoidance in this environment.

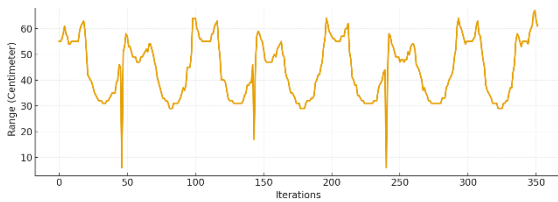


Fig. 9. LiDAR Range Detection

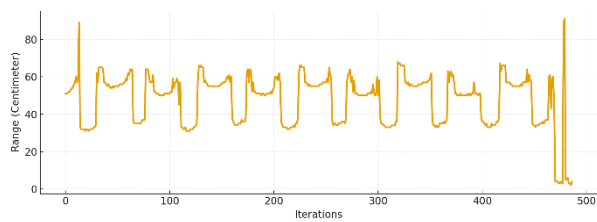


Fig. 10. SONAR Range Detection

Fig. 11 and 12 confirm that LiDAR maintained a low, nearly constant error, whereas SONAR exhibited both a higher bias and large regime-to-regime swings across 352 LiDAR and 487 SONAR samples collected in the box test. Notably, SONAR exceeded 15% error in 36% of iterations and 20% in 26%, while LiDAR never exceeded 10%. At a 40 cm avoidance threshold, this translates to $\pm 3.6\text{ cm}$ worst-case (LiDAR, 9%) vs $\pm 12\text{ cm}$ (SONAR, 29%), materially impacting false triggers and stopping distance. The evidence indicates LiDAR provides the more reliable ranging signal for obstacle avoidance in this environment.

We validated the perception pipeline in a software-in-the-loop city-canyon scene (Simulink dynamics, Unreal visualization). The LiDAR point-cloud frames reconstruct building and curb lines with clear linear segments; loop closures at the central intersection reduce accumulated drift in the pose graph. The error vs time trace appears in fig. 13. The map quality is limited primarily by shallow-incidence returns along long obstacles and by brief scan-matcher slips during turns; loop-closure acceptance pulls the estimate back toward the canonical street grid, yielding bounded drift over multi-block circuits.

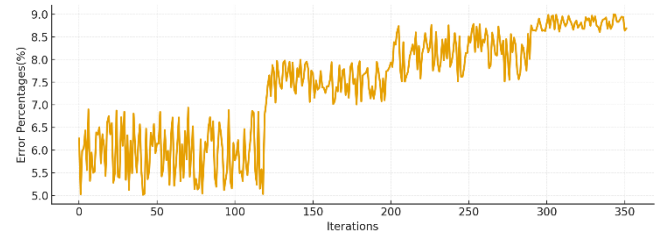


Fig. 11. Error percentages of LiDAR

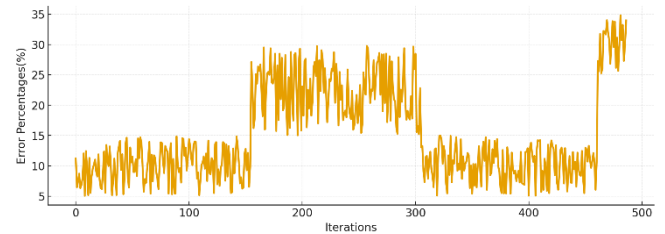


Fig. 12. Error Percentage of SONAR

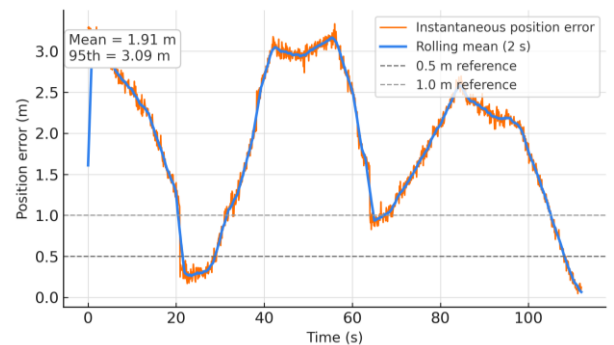


Fig. 13. SLAM Position error over time with a rolling-mean band

IV. CONCLUSION

Limited, reliable perception remains the gating factor for micro-UAV autonomy indoors without GNSS. This work presented a compact 360° scanning head and a sectorized distance-to-PWM hazard law that convert raw range returns into bounded roll/pitch overrides with an explicit latency budget. In a reflective box arena, LiDAR produced stable polar occupancies and consistent scan-to-scan convergence, while ultrasonic sensing suffered fragmented arcs and multipath outliers; a city-canyon SLAM validation further showed that 2D LiDAR yields usable drift behavior with loop-closure recovery for mapping at turn points. Together, these results provide practical guidance: favor 2D LiDAR when precise avoidance and mapping are required, and reserve sonar for tightly constrained compute/power budgets with conservative safety margins. We detail the arbitration logic, thresholds and PWM ranges to enable reproduction on similar airframes. Experiments in a reflective box amplify acoustic multipath and specular LiDAR dropouts relative to open rooms; small panel misalignments bias sectors; and time-base drift between scanner and logger can smear revolution boundaries (mitigated by Hall indexing). These factors bound external validity but stress the sensing stack in a worst-case setting.

REFERENCES

- [1] R. Ahmed and K. H. Mahmud, "Potentiality of high-resolution topographic survey using unmanned aerial vehicle in Bangladesh," *Remote Sens Appl*, vol. 26, p. 100729, Apr. 2022, doi: 10.1016/j.rsase.2022.100729.
- [2] A. M. Muhammad Kamarulzaman, W. S. Wan Mohd Jaafar, M. N. Mohd Said, S. N. M. Saad, and M. Mohan, "UAV Implementations in Urban Planning and Related Sectors of Rapidly Developing Nations: A Review and Future Perspectives for Malaysia," *Remote Sens (Basel)*, vol. 15, no. 11, p. 2845, May 2023, doi: 10.3390/rs15112845.
- [3] N. Hossein Motlagh *et al.*, "Unmanned Aerial Vehicles for Air Pollution Monitoring: A Survey," *IEEE Internet Things J*, vol. 10, no. 24, pp. 21687–21704, Dec. 2023, doi: 10.1109/JIOT.2023.3290508.
- [4] A. Iqbal, M. S. Mondal, W. Veerbeek, M. S. A. Khan, and H. Hakvoort, "Effectiveness of <sc>UAV</sc>-based <sc>DTM</sc> and satellite-based <sc>DEMs</sc> for local-level flood modeling in <sc>Jamuna</sc> floodplain," *J Flood Risk Manag*, vol. 16, no. 4, Dec. 2023, doi: 10.1111/jfr3.12937.
- [5] M. M. Ahmed *et al.*, "An experimental analysis of outdoor UAV localisation through diverse estimators and crowd-sensed data fusion," *Physical Communication*, vol. 66, p. 102475, Oct. 2024, doi: 10.1016/j.phycom.2024.102475.
- [6] M. Yaqot and B. C. Menezes, "Unmanned Aerial Vehicle (UAV) in Precision Agriculture: Business Information Technology Towards Farming as a Service," in *2021 1st International Conference on Emerging Smart Technologies and Applications (eSmarTA)*, IEEE, Aug. 2021, pp. 1–7. doi: 10.1109/eSmarTA52612.2021.9515736.
- [7] A. Hussain, F. Akhtar, Z. H. Khand, A. Rajput, and Z. Shaukat, "Complexity and Limitations of GNSS Signal Reception in Highly Obstructed Environments," *Engineering, Technology & Applied Science Research*, vol. 11, no. 2, pp. 6864–6868, Apr. 2021, doi: 10.48084/etasr.3908.
- [8] J. R. van der Merwe *et al.*, "GNSS interference monitoring and characterisation station," in *2017 European Navigation Conference (ENC)*, IEEE, May 2017, pp. 170–178. doi: 10.1109/EURONAV.2017.7954206.
- [9] X. Zhou, X. Zhang, X. Yang, J. Zhao, Z. Liu, and F. Shuang, "Towards UAV Localization in GNSS-Denied Environments: The SatLoc Dataset and a Hierarchical Adaptive Fusion Framework," *Remote Sens (Basel)*, vol. 17, no. 17, p. 3048, Sep. 2025, doi: 10.3390/rs17173048.
- [10] Y. Gu, L.-T. Hsu, and S. Kamijo, "Passive Sensor Integration for Vehicle Self-Localization in Urban Traffic Environment," *Sensors*, vol. 15, no. 12, pp. 30199–30220, Dec. 2015, doi: 10.3390/s151229795.
- [11] C. K. Toth, Z. Koppányi, V. Navratil, and D. Grejner-Brzezinska, "GEOREFERENCING IN GNSS-CHALLENGED ENVIRONMENT: INTEGRATING UWB AND IMU TECHNOLOGIES," *The International Archives of the Photogrammetry, Remote Sensing and Spatial Information Sciences*, vol. XLII-1/W1, pp. 175–180, May 2017, doi: 10.5194/isprs-archives-XLII-1-W1-175-2017.
- [12] F. Orjales, J. Losada-Pita, A. Paz-Lopez, and Á. Deibe, "Towards Precise Positioning and Movement of UAVs for Near-Wall Tasks in GNSS-Denied Environments," *Sensors*, vol. 21, no. 6, p. 2194, Mar. 2021, doi: 10.3390/s21062194.
- [13] C. Cadena *et al.*, "Past, Present, and Future of Simultaneous Localization and Mapping: Toward the Robust-Perception Age," *IEEE Transactions on Robotics*, vol. 32, no. 6, pp. 1309–1332, Dec. 2016, doi: 10.1109/TRO.2016.2624754.
- [14] W. Hess, D. Kohler, H. Rapp, and D. Andor, "Real-time loop closure in 2D LIDAR SLAM," in *2016 IEEE International Conference on Robotics and Automation (ICRA)*, IEEE, May 2016, pp. 1271–1278. doi: 10.1109/ICRA.2016.7487258.
- [15] R. Mur-Artal, J. M. M. Montiel, and J. D. Tardos, "ORB-SLAM: A Versatile and Accurate Monocular SLAM System," *IEEE Transactions on Robotics*, vol. 31, no. 5, pp. 1147–1163, Oct. 2015, doi: 10.1109/TRO.2015.2463671.
- [16] J. Engel, J. Sturm, and D. Cremers, "Semi-dense Visual Odometry for a Monocular Camera," in *2013 IEEE International Conference on Computer Vision*, IEEE, Dec. 2013, pp. 1449–1456. doi: 10.1109/ICCV.2013.183.
- [17] M. Kaess, H. Johannsson, R. Roberts, V. Ila, J. J. Leonard, and F. Dellaert, "iSAM2: Incremental smoothing and mapping using the Bayes tree," *Int J Rob Res*, vol. 31, no. 2, pp. 216–235, Feb. 2012, doi: 10.1177/0278364911430419.
- [18] P. Geneva, K. Eickenhoff, W. Lee, Y. Yang, and G. Huang, "OpenVINS: A Research Platform for

Visual-Inertial Estimation,” in *2020 IEEE International Conference on Robotics and Automation (ICRA)*, IEEE, May 2020, pp. 4666–4672. doi: 10.1109/ICRA40945.2020.9196524.

- [19] L. Prange *et al.*, “CODE’s five-system orbit and clock solution—the challenges of multi-GNSS data analysis,” *J Geod*, vol. 91, no. 4, pp. 345–360, Apr. 2017, doi: 10.1007/s00190-016-0968-8.
- [20] A. D. Ames, S. Coogan, M. Egerstedt, G. Notomista, K. Sreenath, and P. Tabuada, “Control Barrier

Functions: Theory and Applications,” in *2019 18th European Control Conference (ECC)*, IEEE, Jun. 2019, pp. 3420–3431. doi: 10.23919/ECC.2019.8796030.

- [21] Z. Zhang, Y. Wu, J. Jiang, N. Zheng, and W. Meng, “Realization of Robust Formation for Multi-UAV Systems Using Control Barrier Functions,” *Unmanned Systems*, vol. 13, no. 03, pp. 737–751, May 2025, doi: 10.1142/S2301385025500451.